

# Robust Magnetic Polaron Percolation in the Antiferromagnetic CMR System EuCd<sub>2</sub>P<sub>2</sub>

Marvin Kopp,<sup>1,\*</sup> Charu Garg,<sup>1</sup> Sarah Krebber,<sup>1</sup> Kristin Kliemt,<sup>1</sup> Cornelius Krellner,<sup>1</sup> Sudhaman R. Balguri,<sup>2</sup> Mira Mahendru,<sup>2</sup> Fazel Tafti,<sup>2</sup> Theodore L. Breeze,<sup>3</sup> Nathan P. Bentley,<sup>3</sup> Francis L. Pratt,<sup>4</sup> Thomas J. Hicken,<sup>5</sup> Hubertus Luetkens,<sup>5</sup> Jonas A. Krieger,<sup>5</sup> Stephen J. Blundell,<sup>6</sup> Tom Lancaster,<sup>3</sup> M. Victoria Ale Crivillero,<sup>7</sup> Steffen Wirth,<sup>7</sup> and Jens Müller<sup>1,†</sup>

<sup>1</sup>*Physikalisches Institut, Goethe-University Frankfurt  
Max-von-Laue Str. 1, 60438 Frankfurt am Main, Germany*

<sup>2</sup>*Department of Physics, Boston College*

<sup>3</sup>*140 Commonwealth Avenue, Chestnut Hill, MA 02467, USA*

<sup>4</sup>*Department of Physics, Durham University, Durham, DH1 3LE, United Kingdom*

<sup>5</sup>*ISIS Facility, STFC-Rutherford Appleton Laboratory,*

*Harwell Science and Innovation Campus, Didcot, OX11 0QX, United Kingdom*

<sup>6</sup>*PSI Center for Neutron and Muon Sciences, 5232 Villigen PSI, Switzerland*

<sup>7</sup>*Department of Physics, Oxford University, Clarendon Laboratory, Parks Road, Oxford, OX1 3PU, UK*

<sup>7</sup>*Max-Planck-Institute for Chemical Physics of Solids*

*Nöthnitzer Str. 40, 01187 Dresden, Germany*

(Dated: January 9, 2026)

## I. SUPPLEMENTARY INFORMATION

### A. Sample analysis

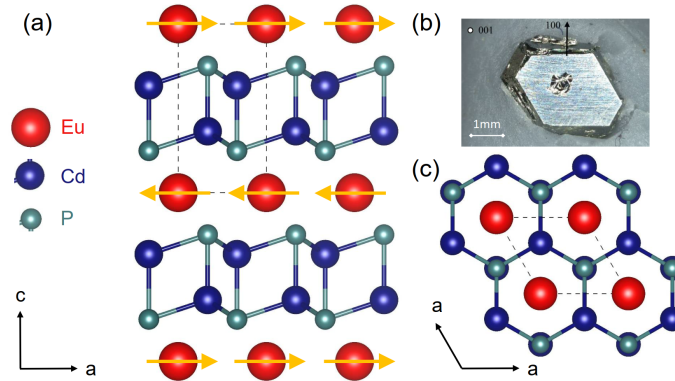


FIG. S1. Structure of EuCd<sub>2</sub>P<sub>2</sub> in (a) and (c) with A-type AFM order indicated by yellow arrows. (b) shows sample #1 after polishing and before gold evaporation and contacting.

The structure and chemical composition of the EuCd<sub>2</sub>P<sub>2</sub> samples was confirmed using powder X-ray diffraction (PXRD), energy dispersive X-ray spectroscopy (EDX) and single crystal analysis. The characterisation of the crystal structure of sample #1 by PXRD yielded lattice parameters of  $a = 4.324 \text{ \AA}$  and  $c = 7.179 \text{ \AA}$ . The powder diffraction patterns were recorded on a diffractometer with a Bragg-Brentano geometry and copper  $K_{\alpha}$  radiation (Bruker D8). The chemical composition of sample #1 was analysed with EDX, yielding averaged values of Eu =  $(17 \pm 2) \text{ at\%}$ , Cd =  $(40 \pm 2) \text{ at\%}$  and P =  $(43 \pm 2) \text{ at\%}$ . Analysis of sample #2 yielded similar results within the error range.

In Tab. S1 we provide a comparison of various parameters relevant for the magnetotransport properties for different samples reported in the literature and in this work. Interestingly, samples exhibit both metallic or semiconducting

\* kopp@physik.uni-frankfurt.de

† j.mueller@physik.uni-frankfurt.de

30 behavior upon cooling from room temperature and a significant range of charge carrier concentration  $n_c$ . Previous  
 31 reports have established a correlation between higher charge densities and Eu vacancies, suggesting the possibility of  
 32 intrinsic doping [3]. Samples reported in [3] are even metals with low  $\rho(300\text{ K})$  and a positive coefficient  $d\rho/dT > 0$   
 33 down to low temperatures where FM ordering occurs, highlighting the strong competition between FM and AFM  
 34 interactions in this material. The magnitude of the CMR and also the ratio  $\rho(T_{\text{peak}})/\rho(300\text{ K})$  systematically increase  
 35 with decreasing  $n_c$ , whereas  $T_{\text{peak}}$  increases with increasing  $n_c$ .

Sample/Data origin	#1 [this work]	#2 [this work]	Wang <i>et al.</i> [1]	Zhang <i>et al.</i> [2]	Chen <i>et al.</i> [3]
$n_c(300\text{ K})$ from Hall	$4.8 \cdot 10^{17}\text{ cm}^{-3}$	$3.5 \cdot 10^{18}\text{ cm}^{-3}$	$-6 \cdot 10^{18}\text{ cm}^{-3}$	$\sim 1 \cdot 10^{17}\text{ cm}^{-3}$	$4.6 \cdot 10^{19}\text{ cm}^{-3}$ (at 150 K)
$\rho(300\text{ K})$	$2.3 \cdot 10^{-1}\text{ }\Omega\text{cm}$	$1.4\text{ }\Omega\text{cm}$	$2.4 \cdot 10^{-2}\text{ }\Omega\text{cm}$	$3.1 \cdot 10^{-1}\text{ }\Omega\text{cm}$	$5.5 \cdot 10^{-3}\text{ }\Omega\text{cm}$
high- $T$ behavior	semiconducting	semiconducting	metallic	n.a.	metallic
$\rho(T_{\text{peak}})/\rho(300\text{ K})$	$1.33 \cdot 10^4$	$1.46 \cdot 10^3$	$5 \cdot 10^1$	$5 \cdot 10^3$	0.87
$T_{\text{peak}}$	14 K	15 K	18 K	14 K	47 K
$T_{\text{N}}$	11 K	11 K	11 K	10.9 K	$T_{\text{C}} = 47\text{ K}$
$\text{MR}_{\text{max}}$	$2.5 \cdot 10^5\%$ (14 K, 5 T)	$3.5 \cdot 10^4\%$ (16 K, 5 T)	$5.6 \cdot 10^3\%$ (18 K, 5 T)	$1.75 \cdot 10^5\%$ (14 K, 2 T)	80% (47 K, 5 T)
$\mu(300\text{ K}) = (\rho n_c)^{-1}$	$56\text{ cm}^2/\text{Vs}$	$1.3\text{ cm}^2/\text{Vs}$	$-43.3\text{ cm}^2/\text{Vs}$	$\sim 200\text{ cm}^2/\text{Vs}$	$24.6\text{ cm}^2/\text{Vs}$

TABLE S1. Properties of different  $\text{EuCd}_2\text{P}_2$  samples. Zhang *et al.* report sample-to-sample dependencies and some information is not available (n.a.).

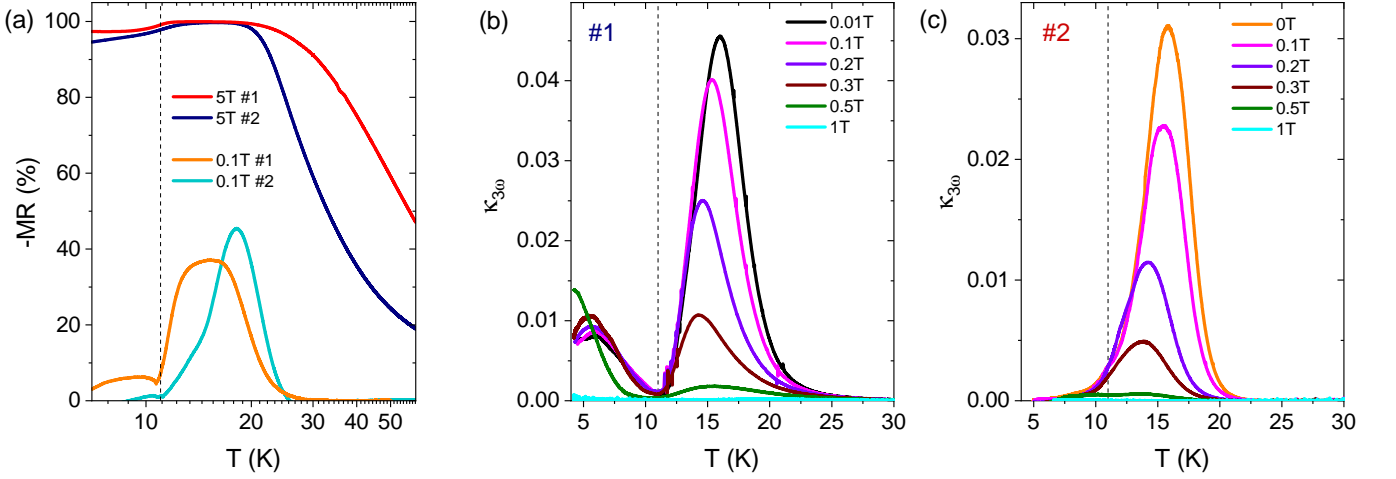


FIG. S2. (a) Negative magnetoresistance  $-MR = -(\rho(B) - \rho(0))/\rho(0)$  at relatively small ( $\mu_0 H = 0.1$  T) and large fields  $\mu_0 H = 5$  T for both samples #1 (in orange and red) and #2 (in light blue and blue). (b,c) Fourier coefficient  $\kappa_{3\omega} = V_{3\omega}/V_{1\omega}$  of the third-harmonic voltage generation below  $T = 30$  K for sample #1 and #2 measured in magnetic fields from  $\mu_0 H = 0$  T to 1 T.

### B. Weakly-nonlinear resistance and noise

Besides the common resistance calculated by Ohm's law  $R = V/I$ , assuming a linear dependence between current  $I$  flowing through, and voltage drop  $V$  across the sample, in spatially inhomogeneous systems it is often useful to consider so-called higher harmonics of the voltage signal. Prime examples for intrinsic electronic and/or magnetic phase separation are the vortex lattice in a type-II superconductor, the magnetic skyrmion lattice, coexistence of phases near a first-order phase transition or the emergence of nano-scale clusters (e.g. polar nanoregions in relaxor ferroelectrics or magnetic polarons in CMR systems) [4–10]. The latter two examples are often discussed in the context of percolation in a random resistor network (RRN) [11, 12]. Basic ideas of such a scenario are often invoked to describe the dynamics of magnetic polarons in CMR systems [13, 14].

In a model percolation system of a semicontinuous metal film [15], upon application of an AC current ( $I = I_0 \cos(\omega t)$ ) the local resistance  $r_\alpha$  can be written as

$$r_\alpha = r_0 + \delta r_\alpha \cos(2\omega t + \phi), \quad (1)$$

where  $\delta r_\alpha$  are the fluctuations of each local resistance assumed to be significantly smaller than their resistance  $r_0$  and  $\phi$  is the phase shift between the heat production and the local temperature. The voltage across the sample can be written as

$$V = IR = I_0 R_0 \cos(\omega t) + \frac{1}{2} I_0 \Delta R \cos(3\omega t + \phi). \quad (2)$$

Thus, a third-harmonic voltage

$$V_{3\omega} \propto I_0 \Delta R \propto \frac{\sum i_\alpha^4 r_\alpha^2}{I_0} \quad (3)$$

is created by the sample and connected to the fourth-order distribution of the local currents  $i_\alpha$ . In a simple RNN there is a direct connection to the PSD of the resistance fluctuations:

$$S_R/R^2 \propto \frac{V_{3\omega}}{I_0^3 R^2} \quad (4)$$

Here, energy conservation  $I^2 \Delta R = \sum i_\alpha^2 \delta r_\alpha$  is used and a power-law scaling

$$\frac{V_{3\omega}}{I_0^3} \propto R^{2+w} \quad (5)$$

is expected, where the critical exponent  $w = \kappa/t$  depends on the particular percolation scenario [16, 17].

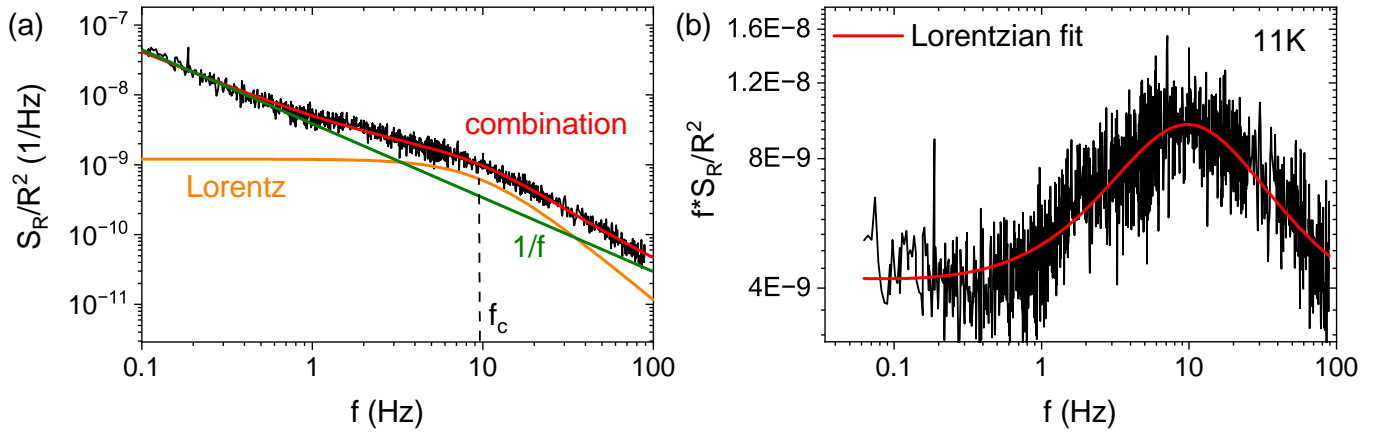


FIG. S3. Typical PSD spectrum  $S_R/R^2(f)$  of a  $1/f$ -type noise (green line) superimposed with a dominating two-level fluctuator producing a Lorentz spectrum (orange) in (a). Plot of  $S_R/R^2 \cdot f$  with a fit (red) to evaluate the amplitude of the  $1/f$ -background, its frequency exponent  $\alpha$ , the amplitude of the Lorentzian and the corner frequency  $f_c$  (b).

56 The generated third-harmonic resistance or so-called weakly-nonlinear transport can be easily accessed in an AC  
 57 lock-in measurement and reveals sensitive information on microscopic inhomogeneities in the current distribution  
 58 of CMR systems [9, 18]. The results are shown in Fig. S2 for #1 in (b) and for #2 in (c). The Fourier coefficient  
 59  $\kappa_{3\omega} = V_{3\omega}/V_{1\omega}$  and is clearly nonzero above  $T_N$  and below about 25 K and shows a pronounced peak for both samples  
 60 at about  $\sim 16$  K in the vicinity of the resistance peak. We note that the observed values of  $\kappa_{3\omega} \sim 3 - 4\%$  in zero  
 61 magnetic field are similarly large as the ones observed for the FM CMR systems  $\text{EuB}_6$  (bulk) [9] and  $(\text{La,Ca})\text{MnO}_3$   
 62 (thin film) [18], where the third-harmonic generation is due to a percolative insulator-metal transition involving  
 63 magnetic polarons.

64 Strikingly, the weakly-nonlinear transport peak is strongly suppressed already in small magnetic fields, with the  
 65 peak shifting to lower temperatures with increasing field, and vanishes between about  $\mu_0 H = 0.5$  T and 1 T for both  
 66 samples. According to the common interpretation outlined above, this means a significant inhomogeneity in the  
 67 microscopic current distribution in a rather well defined temperature interval above  $T_N$ , which becomes suppressed  
 68 in moderate magnetic fields. We note that the temperatures where  $\kappa_{3\omega} \gtrsim 0$  coincides with a finite negative MR at  
 69 low fields and with the plateau-like regime of a large negative MR of more than 99% at higher fields. Again, in  
 70 agreement with the behavior of the MR at smaller fields, for sample 1, a second, smaller peak develops upon cooling  
 71 below  $T_N$ , the magnitude of which changes only slightly in increasing magnetic fields and is only suppressed in this  
 72 temperature regime for fields of order 1 T. Sample 2 does not show such a second peak and the weakly-nonlinear  
 73 transport is close to zero below  $T_N$ .

74  
 75 An exemplary measured power spectral density (PSD)  $S_R/R^2$  of the resistance fluctuations is shown in Fig. S3  
 76 (a) in a double logarithmic plot, where the Lorentzian contribution is shown in blue, the linear  $1/f$  background  
 77 in red and the resulting combination in orange, describing the measured spectrum in black. Also marked is the  
 78 corner frequency  $f_c$  of the Lorentzian spectrum, which is connected to the lifetimes of the two-level fluctuator by  
 79  $f_c = 1/(2\pi) \cdot (1/\tau_1 = 1/\tau_2)$ . By plotting  $S_R/R^2 \cdot f$  as shown in (b), one can fit the spectrum with a Lorentzian  
 80 function and obtain the amplitude and slope of the  $1/f$  contribution, as well as the corner frequency  $f_c$  and the  
 81 amplitude of the Lorentzian contribution.

82  
 83 In a percolation scenario a power-law dependence  $B = V_{3\omega}/I^3 \propto R^{2+w}$  should be observed for the weakly nonlinear  
 84 resistance [15]. As shown in Fig. S4 the data can be linearly fitted between  $T = 18$  K and  $T = 15$  K yielding  $w = 1.24$   
 85 very similar to the observation in silver thin films (or  $w = 0.53$  for  $T < 15$  K). A fit in the same temperature range  
 86 for  $S_R/R^2(f = 1 \text{ Hz})$  plotted versus  $R(T)$  yields a larger  $w = 4.4$  but also with a much larger error  $\pm 0.7$  as the fit is  
 87 worse and there are less points to average over (or  $w = 1.18 \pm 0.47$  below  $T = 15$  K). In theory the scaling should  
 88 also be  $S_R/R^2 \propto R^w$ . It should be mentioned, that scaling of the third-harmonic signal with current and frequency,  
 89 as well as basic scaling relations of the noise PSD expected for simple RRNs do not yield the same results for the  
 90 present system, but vary with the chosen temperature range, which likely is due to the intricate interplay between  
 91 competing AFM and FM interactions in  $\text{EuCd}_2\text{P}_2$  (see Fig. S4).

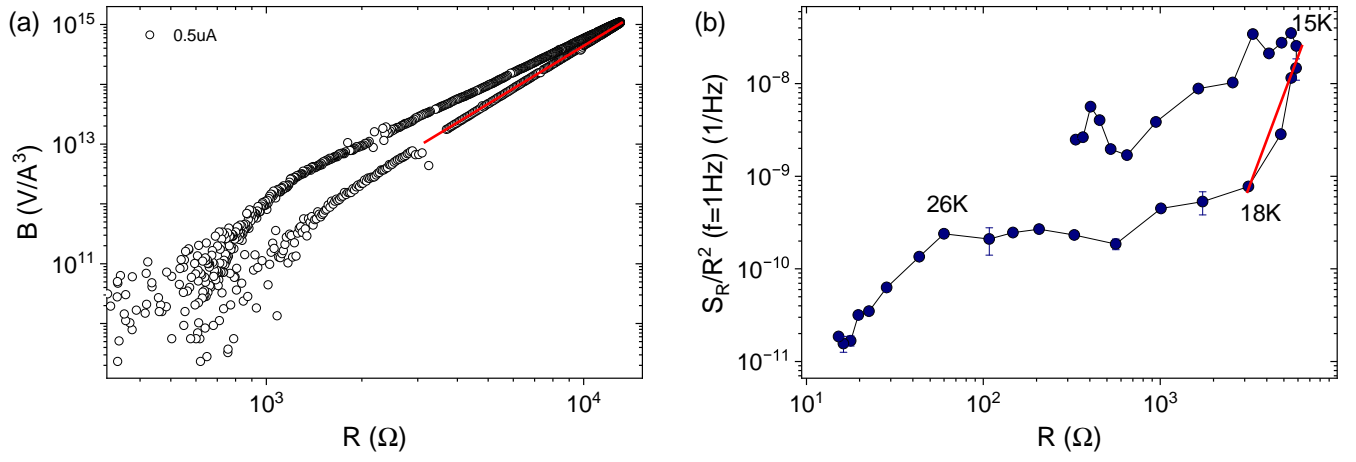


FIG. S4. Plot of the normalized third-harmonic amplitude  $B(T) = V_{3\omega}(T)/I^3$  versus the linear resistance  $R(T)$  on a double logarithmic scale (a). The data can be linearly fitted between  $T = 18 \text{ K}$  and  $T = 15 \text{ K}$  yielding  $w = 1.24$ . A fit in the same temperature range for  $S_R/R^2$  ( $f = 1 \text{ Hz}$ ) plotted versus  $R(T)$  (b) yields a larger  $w = 4.4$  but also with a much larger error  $\pm 0.7$ .

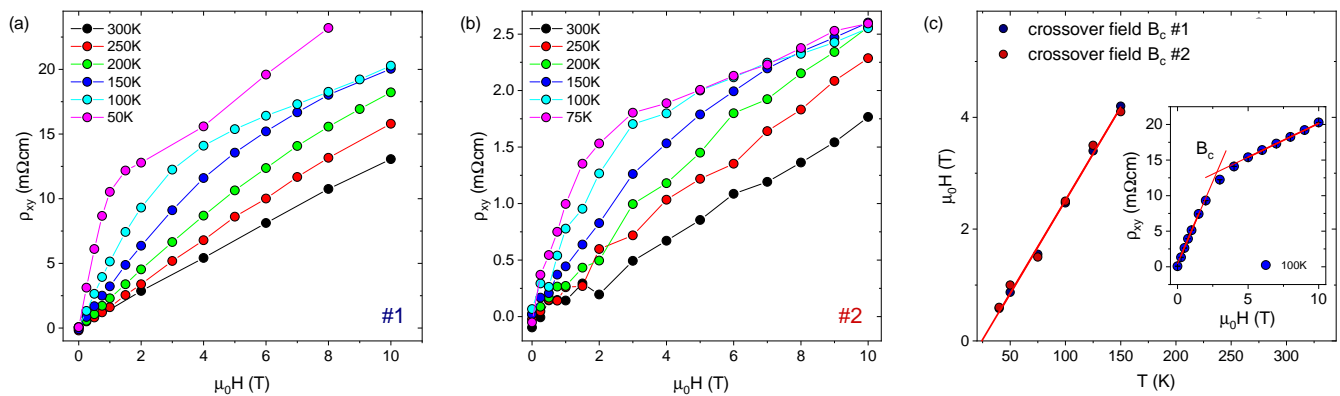


FIG. S5. (a) Hall resistivity  $\rho_{xy}$  measured at distinct temperatures are shown for sample #1 and #2 in (b). The linear behavior at high temperatures develops into a curved shape upon cooling with two distinct slopes at low and high magnetic fields. Lines are guides to the eyes. (c) Crossover field  $B_c$  where the two slopes intersect, shown for both samples #1 and #2 in blue and red, respectively. Inset shows the construction at  $T = 100$  K.

94

### C. Magnetic and magnetotransport measurements

95 Hall measurements were carried out on the same samples #1 and #2 using the given contact geometry. In order  
 96 to cancel out the magnetoresistance offset due to the non-perfect Hall cross geometry, voltages have been measured  
 97 at discrete positive and negative magnetic fields antisymmetrized.

98 Figure S5(a) displays the Hall resistivity  $\rho_{xy}$  vs.  $\mu_0 H$  up to 10 T for various discrete temperatures from  $T = 300$  K  
 99 down to 50 K for sample #1, see SI Fig. S5 for the data of #2. The temperature profiles for both samples are  
 100 rather similar, despite the about one order of magnitude larger slope at room temperature (and correspondingly lower  
 101 carrier concentration) of #1, see inset of Fig. 1(b). In particular, the almost perfect scaling of the crossover field  
 102  $B_c$  for both samples shown in Fig. S5(c), together with the power-law scaling of the weakly-nonlinear transport as  
 103 evidence for dynamic percolation, Fig. S4(a), and the strong magnetic field dependence of the electrical transport,  
 104 rules out extrinsic effects like structural/chemical inhomogeneities.

105 In order to compare low-frequency resistance and magnetic fluctuations we measured the frequency-dependent AC  
 106 susceptibility of sample #2. Figure S6(a) shows the real part  $\chi'(T, f)$  measured at zero external DC field with an AC  
 107 field of 5 Oe applied along the  $c$ -axis for different frequencies (yellow to red colors) in comparison to the data taken at  
 108  $\mu_0 H = 5$  T dc field (blue) for  $f = 17$  Hz. For decreasing temperature the susceptibility shows the expected behavior  
 109 for an antiferromagnet with an essentially frequency-independent cusp marking the magnetic transition temperature  
 110  $T_N = 11$  K and further decrease in the AFM phase. The jump at  $T = 3.7$  K is due to the superconducting transition of  
 111 Sn flux incorporated in to the sample during the crystal growth. In a magnetic field of 5 T the susceptibility decreases  
 112 below about  $T = 40$  K reaching zero below  $T = 17$  K.

113 The imaginary part of the AC susceptibility  $\chi''(T)$  is shown in Fig. S6(b) for frequencies  $f = 17 - 477$  Hz. The  
 114 magnitude of  $\chi''(T)$  with a sharp peak at  $T_N = 11.1$  K is frequency dependent with larger values for higher frequencies.  
 115 (The anomaly at  $T = 3.7$  K is due to the superconducting transition of Sn flux incorporated in the sample during  
 116 crystal growth.)

117 In the inset of Fig. S6(a) the anisotropy  $\gamma(T) = \chi'_{001}(T)/\chi'_{210}(T)$  for the AC field along the  $c$ -axis (hard axis) and  
 118 within the  $a$ - $a$  plane (easy axis) is shown. We find  $\gamma(T) \approx 1$  (dotted line) at high temperatures while it starts to  
 119 gradually decrease upon cooling until a sharp downturn occurs below  $T \approx 25$  K, i.e. the susceptibility for the field  
 120 applied in the  $a$ - $a$  plane is increasing faster and becomes larger than for the  $c$ -direction. Below the magnetic ordering  
 121 temperature, the anisotropy in the zero-field magnetic susceptibility saturates at a value of  $\gamma \sim 0.14$ .

122 In the inset of Fig. S6(c) the calculated  $S_M(f)$  at  $T = 11.2$  K is shown to follow a  $1/f^\alpha$  frequency dependence with  
 123  $\alpha = 0.98$ , allowing a direct comparison to the resistance noise measurements which we present in the discussion  
 124 chapter.  
 125

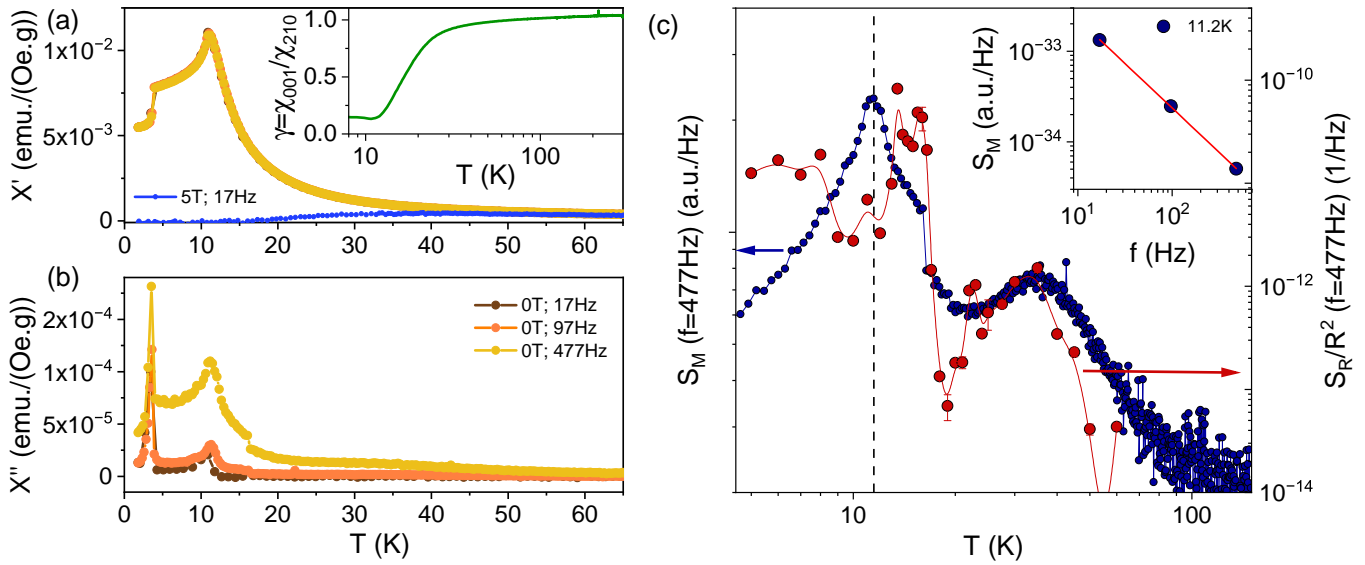


FIG. S6. (a) Real part of the AC susceptibility  $\chi'$  of sample #2 at zero dc magnetic field for various frequencies between  $f = 0.97$  Hz and  $f = 477$  Hz. Data at 17 Hz measured in an external dc field of  $\mu_0 H = 5$  T are shown in blue. The amplitude of the AC field is  $\mu_0 H = 0.5$  mT. Inset shows the anisotropy  $\gamma(T) = \chi'_{001}(T)/\chi'_{210}(T)$ , i.e. the ratio of the zero dc field susceptibilities with the AC field along the  $c$ -axis and within the  $a$ - $a$  plane. (b) Imaginary part  $\chi''$  with the same colour code for different frequencies. (c) Comparison of the calculated magnetic noise PSD  $S_M(f = 477$  Hz) (blue) and the measured resistance noise PSD  $S_R/R^2(f = 477$  Hz) (red). Inset demonstrates the  $1/f$  dependence of the magnetic noise at  $T = 11.2$  K.

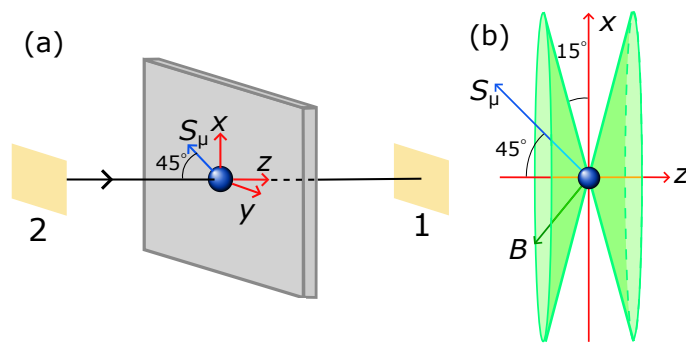


FIG. S7. The geometry of our  $\mu$ SR experiments made at  $S\mu S$ . (a) The detector setup, showing the initial muon spin orientation relative to the beam direction and the forwards (1) and backwards (2) detectors. (b) The cone of possible local dipole fields,  $B$ , at the muon stopping site, resulting in a range of possible angles,  $\phi$ , between the muon spin and the local field.

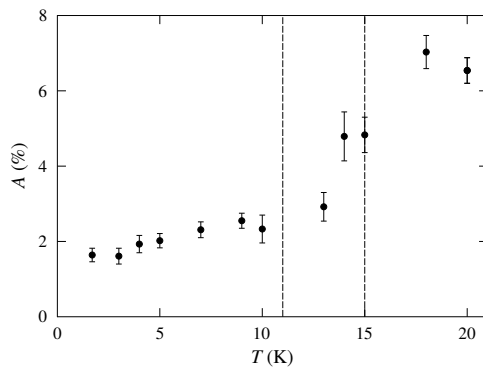


FIG. S8. (a) The amplitude,  $A$ , of the asymmetry component in our wTF experiments at  $S\mu S$  corresponding to oscillations in an applied field.

126

#### D. Muon-spin relaxation

127 The ZF  $\mu$ SR data measured at  $S\mu S$  is made up of two components at temperatures below  $T_N$ : an oscillating term  
 128 with an asymmetry of  $A = 9.0\%$  and a constant term with  $A = 4.7\%$ . We made weak transverse field (wTF)  
 129 measurements at  $S\mu S$  where a field of 3 mT is directed along the  $x$ -direction in Fig. S7(a), which allow us to observe  
 130 the response of muon spins in magnetically disordered environments. The amplitude of the nonmagnetic asymmetry  
 131 component is plotted against temperature in Fig. S8 and shows an amplitude of 1.5% at the lowest temperature point.  
 132 This contribution could be either a background due to muons stopping outside the sample or a behavior intrinsic to the  
 133 material, implying the existence of a small nonmagnetic volume fraction at low temperatures. In the absence of any  
 134 other evidence for the latter case, we assume that this term represents a 1.5% background in all of our data collected  
 135 at  $S\mu S$ . The amplitude of the constant term in the ZF data with this background subtracted is therefore 3.2%. The  
 136 oscillating term corresponds to the precession of the component of the muon spin that is perpendicular to the local  
 137 field, and therefore, in a single crystal sample, has an amplitude proportional to the sine squared of the spin-field  
 138 angle,  $\phi$ . The constant term corresponds to the component of the muon spin that is pinned parallel to the local field,  
 139 and so has an amplitude proportional to  $\cos^2 \phi$ . The ratio of the two is therefore  $\tan^2 \phi = 9.0/3.2 = 2.8 \pm 0.99$  or  
 140  $\phi = 59 \pm 5^\circ$ .

141 As part of our analysis of the  $\mu$ SR data we carried out DFT calculations to identify a candidate muon stopping site  
 142 at a single low energy position within the unit cell (as discussed in Section IV D). We were able to then calculate the  
 143 local dipole field experienced by muons stopping at this site, which is found to be pointed  $15^\circ$  out of the  $a-a$  plane. In  
 144 our experiments the spins of the incoming muons were polarized at an angle of  $45^\circ$  to their direction of travel towards  
 145 the sample (the  $z$  axis), as shown in Fig. S7(a). The sample was positioned such that the crystallographic  $c$  axis was  
 146 orientated along  $z$ , so that the local dipole field at the muon site must exist on a cone about the  $z$  axis depending on  
 147 the crystal orientation in the  $a-a$  plane as shown in Fig. S7(b). The minimum spin-field angle is therefore  $\phi = 30^\circ$ ,  
 148 so that  $0.33 \leq \tan^2 \phi \leq \infty$ , compatible with our estimate of  $\phi = 59^\circ$  from the data. This is complicated slightly  
 149 by the fact that in our experiments we used a mosaic made up of single crystals oriented in this way. The resulting

averaging over angles in the  $a - a$  plane gradually constrains this range with increasing crystal number, approaching an expected value of 1.14 [19], but for a small number our observed ratio of 2.8 is reasonable.

Over the temperature region  $T_N < T < T^*$  the total asymmetry rises from 13.7% to 16.6%. Accounting for a background of 1.5%, this gives sample-only asymmetries of 12.2% and 15.1% respectively. The  $45^\circ$  rotation of the initial muon spin away from the detector axis means that the total initial asymmetry is reduced by a factor of  $\sqrt{2}$ , so at high temperatures  $16.6\% \times \sqrt{2} = 23.5\%$  is in good agreement with the expected total asymmetry on the FLAME instrument. This suggests that we are observing the full asymmetry from all stopped muons in the high-temperature region, but that at low temperatures there is a phase accounting for  $0.19 \pm 0.02$  of the total sample volume whose contribution is not observed in the asymmetry, presumably because the spins in this magnetic environment are relaxed so quickly that they are not resolved in our data.

Our wTF measurements show an increase of about 4.5% above  $T_N$ . This corresponds to a total volume fraction of  $0.30 \pm 0.06$  undergoing a phase transition from magnetic order to nonmagnetic disorder. The rest of the muon sites from the ordered phase therefore enter a dynamically fluctuating magnetic phase that strongly relaxes the muon spins.

- 
- [1] Z. Wang, J. D. Rogers, X. Yao, R. Nichols, K. Atay, B. Xu, J. Franklin, I. Sochnikov, P. J. Ryan, D. Haskel, and F. Tafti, Colossal Magnetoresistance without Mixed Valence in a Layered Phosphide Crystal, *Advanced Materials* **33**, 2005755 (2021).
- [2] H. Zhang, F. Du, X. Zheng, S. Luo, Y. Wu, H. Zheng, S. Cui, Z. Sun, Z. Liu, D. Shen, M. Smidman, Y. Song, M. Shi, Z. Zhong, C. Cao, H. Yuan, and Y. Liu, Electronic band reconstruction across the insulator-metal transition in colossally magnetoresistive  $\text{EuCd}_2\text{P}_2$ , *Phys. Rev. B* **108**, L241115 (2023).
- [3] X. Chen, Z. Wang, Z. Zhou, W. Yang, Y. Liu, J.-Y. Lu, Z. Ren, G.-H. Cao, F. Tafti, S. Dong, and Z.-C. Wang, Manipulating magnetism and transport properties of  $\text{EuCd}_2\text{P}_2$  with a low carrier concentration, *Physical Review B* **109** (2024).
- [4] G. Blatter, M. V. Feigel'man, V. B. Geshkenbein, A. I. Larkin, and V. M. Vinokur, Vortices in high-temperature superconductors, *Rev. Mod. Phys.* **66**, 1125 (1994).
- [5] N. Nagaosa and Y. Tokura, Topological properties and dynamics of magnetic skyrmions, *Nature Nanotechnology* **8**, 899 (2013).
- [6] T. Thomas, Y. Agarmani, S. Hartmann, M. Kartsovnik, N. Kushch, S. M. Winter, S. Schmid, P. Lunkenheimer, M. Lang, and J. Müller, Slow and non-equilibrium dynamics due to electronic ferroelectricity in a strongly-correlated molecular conductor, *npj Spintronics* **2** (2024).
- [7] P.-G. de Gennes, Effects of Double Exchange in Magnetic Crystals, *Physical Review* **118**, 141 (1960).
- [8] T. Kasuya and A. Yanase, Anomalous Transport Phenomena in Eu-Chalcogenide Alloys, *Reviews of Modern Physics* **40**, 684 (1968).
- [9] P. Das, A. Amyan, J. Brandenburg, J. Müller, P. Xiong, S. von Molnár, and Z. Fisk, Magnetically driven electronic phase separation in the semimetallic ferromagnet  $\text{EuB}_6$ , *Phys. Rev. B* **86**, 184425 (2012).
- [10] M. Pohlit, S. Rößler, Y. Ohno, H. Ohno, S. von Molnár, Z. Fisk, J. Müller, and S. Wirth, Evidence for Ferromagnetic Clusters in the Colossal-Magnetoresistance Material  $\text{EuB}_6$ , *Physical Review Letters* **120**, 10.1103/physrevlett.120.257201 (2018).
- [11] R. Rammal, C. Tannous, P. Breton, and A.-M. S. Tremblay, Flicker ( $1/f$ ) Noise in Percolation Networks: A New Hierarchy of Exponents, *Phys. Rev. Lett.* **54**, 1718 (1985).
- [12] D. Stauffer and A. Aharony, *Introduction To Percolation Theory* (Taylor & Francis, 2018).
- [13] L. P. Gor'kov and V. Z. Kresin, Properties of Manganites: Band and Percolation Approaches, *Journal of Superconductivity* **12**, 243 (1999).
- [14] A. Kaminski and S. D. Sarma, Polaron Percolation in Diluted Magnetic Semiconductors, *Physical Review Letters* **88**, 10.1103/physrevlett.88.247202 (2002).
- [15] Y. Yagil and G. Deutscher, Third-harmonic generation in semicontinuous metal films, *Phys. Rev. B* **46**, 16115 (1992).
- [16] A.-M. S. Tremblay, S. Feng, and P. Breton, Exponents for  $1/f$  noise, near a continuum percolation threshold, *Physical Review B* **33**, 2077 (1986).
- [17] S. Kogan, *Electronic noise and fluctuations in solids* (Cambridge University Press, 1996).
- [18] V. Moshnyaga, K. Gehrke, O. I. Lebedev, L. Sudheendra, A. Belenchuk, S. Raabe, O. Shapoval, J. Verbeeck, G. V. Tendeloo, and K. Samwer, Electrical nonlinearity in colossal magnetoresistance manganite films: Relevance of correlated polarons, *Phys. Rev. B* **79**, 134413 (2009).
- [19] J. Graham, T. Hicken, R. Regmi, M. Janoschek, I. Mazin, H. Luetkens, N. Ghimire, and Z. Guguchia, Local probe evidence supporting altermagnetism in  $\text{Co}_{1/4}\text{NbSe}_2$ , arXiv preprint arXiv:2503.09193 (2025).